Journal of Astronomical Telescopes, Instruments, and Systems

AstronomicalTelescopes.SPIEDigitalLibrary.org

SAXO: the extreme adaptive optics system of SPHERE (I) system overview and global laboratory performance

Jean-Francois Sauvage
Thierry Fusco
Cyril Petit
Anne Costille
David Mouillet
Jean-Luc Beuzit
Kjetil Dohlen
Markus Kasper
Marcos Suarez
Christian Soenke
Andrea Baruffolo
Bernardo Salasnich
Sylvain Rochat
Enrico Fedrigo
Pierre Baudoz
Emmanuel Hugot
Arnaud Sevin
Denis Perret
Francois Wildi
Mark Downing
Philippe Feautrier
Pascal Puget
Arthur Vigan
Jared O'Neal
Julien Girard
Dimitri Mawet
Hans Martin Schmid
Ronald Roelfsema

Jean-Francois Sauvage, Thierry Fusco, Cyril Petit, Anne Costille, David Mouillet, Jean-Luc Beuzit, Kjetil Dohlen, Markus Kasper, Marcos Suarez, Christian Soenke, Andrea Baruffolo, Bernardo Salasnich, Sylvain Rochat, Enrico Fedrigo, Pierre Baudoz, Emmanuel Hugot, Arnaud Sevin, Denis Perret, Francois Wildi, Mark Downing, Philippe Feautrier, Pascal Puget, Arthur Vigan, Jared O'Neal, Julien Girard, Dimitri Mawet, Hans Martin Schmid, Ronald Roelfsema, "SAXO: the extreme adaptive optics system of SPHERE (I) system overview and global laboratory performance," *J. Astron. Telesc. Instrum. Syst.* **2**(2), 025003 (2016), doi: 10.1117/1.JATIS.2.2.025003.

SPIE.

SAXO: the extreme adaptive optics system of SPHERE (I) system overview and global laboratory performance

Jean-Francois Sauvage,[a,b,*] Thierry Fusco,[a,b] Cyril Petit,[a] Anne Costille,[b] David Mouillet,[c] Jean-Luc Beuzit,[c] Kjetil Dohlen,[b] Markus Kasper,[d] Marcos Suarez,[d] Christian Soenke,[d] Andrea Baruffolo,[e] Bernardo Salasnich,[e] Sylvain Rochat,[c] Enrico Fedrigo,[f] Pierre Baudoz,[g] Emmanuel Hugot,[b] Arnaud Sevin,[g] Denis Perret,[g] Francois Wildi,[h] Mark Downing,[d] Philippe Feautrier,[c] Pascal Puget,[c] Arthur Vigan,[b,d] Jared O'Neal,[d] Julien Girard,[d] Dimitri Mawet,[d] Hans Martin Schmid,[i] and Ronald Roelfsema[j]

[a]ONERA—Optics Department, 29 Avenue de la Division Leclerc, F-92322 Chatillon Cedex, France
[b]Aix Marseille Université, CNRS, Laboratoire d'Astrophysique de Marseille, UMR 7326, 13388 Marseille, France
[c]UJF-Grenoble 1/CNRS-INSU, Institut de Planetologie et d'Astrophysique de Grenoble, UMR 5274, Grenoble F-38041, France
[d]European Southern Observatory, Karl-Schwarzschild-Strasse 2, Garching D-85748, Germany
[e]Istituto Nazionale di Astrofisica, Osservatorio di Padova, Vicolo Osservatorio 5, Padova 35122, Italia
[f]European Patent Office, Bob-van-Benthem-Platz 1, Munich 80469, Germany
[g]Laboratoire d'Etudes Spatiales et d'Instrumentation Astrophysiques—Observatoire de Paris, Section de Meudon 5, place Jules Janssen 92195 Meudon, France
[h]Observatoire de Geneve, 51 Chemin des Maillettes, CH-1290 Sauverny, Switzerland
[i]ETH Zurich, Institute for Astronomy, Wolfgang-Pauli-Strasse 27, CH-8092 Zurich, Switzerland
[j]NOVA Optical Infrared Instrumentation Group, Oude Hoogeveensedijk 4, 7991 PD Dwingeloo, The Netherlands

Abstract. The direct imaging of exoplanet is a leading field of today's astronomy. The photons coming from the planet carry precious information on the chemical composition of its atmosphere. The second-generation instrument, Spectro-Polarimetric High contrast Exoplanet Research (SPHERE), dedicated to detection, photometry and spectral characterization of Jovian-like planets, is now in operation on the European very large telescope. This instrument relies on an extreme adaptive optics (XAO) system to compensate for atmospheric turbulence as well as for internal errors with an unprecedented accuracy. We demonstrate the high level of performance reached by the SPHERE XAO system (SAXO) during the assembly integration and test (AIT) period. In order to fully characterize the instrument quality, two AIT periods have been mandatory. In the first phase at Observatoire de Paris, the performance of SAXO itself was assessed. In the second phase at IPAG Grenoble Observatory, the operation of SAXO in interaction with the overall instrument has been optimized. In addition to the first two phases, a final check has been performed after the reintegration of the instrument at Paranal Observatory, in the New Integration Hall before integration at the telescope focus. The final performance aimed by the SPHERE instrument with the help of SAXO is among the highest Strehl ratio pretended for an operational instrument (90% in H band, 43% in V band in a realistic turbulence r_0, and wind speed condition), a limit R magnitude for loop closure at 15, and a robustness to high wind speeds. The full-width at half-maximum reached by the instrument is 40 mas for infrared in H band and unprecedented 18.5 mas in V band. [DOI: 10.1117/1.JATIS.2.2.025003]

Keywords: adaptive optics; coronagraph; high contrast imaging; wavefront sensing; control; phase diversity; Shack–Hartmann.

Paper 15058 received Jul. 23, 2015; accepted for publication Mar. 31, 2016; published online May 24, 2016.

1 Introduction

The direct imaging of extrasolar planets is one of the most exciting challenges of today's astronomy. From a scientific viewpoint, since the light coming from an extrasolar planet is able to reveal the chemical elements of its atmosphere, direct imaging of exoplanets enables the search for habitable planets and eventually extraterrestrial life. From a philosophical viewpoint, it could bring an answer to the question: are we alone? From an instrumental viewpoint, collecting the few photons coming from the planet and disentangling them from the high flux coming from the star is one of the most difficult tasks ever attempted in astronomy. The last decade has seen the first results[1] on the instrument NACO, with its high contrast mode.[2] The interest of the astrophysical community for this quest can be seen by the multiple high performance XAO system providing high contrast imaging installed all over the world. Among them, we can notice the Palm-3000 system for the 5.1 m Hale telescope at Palomar Observatory,[3] the SceXAO system at Subaru telescope,[4] the MagAO system at 6.5 m Magellan Telescope,[5] or the first light adaptive optics (AO) system at 8-m class large binocular telescope.[6]

The year 2014 saw a real revolution with the delivery of two instruments fully dedicated to high contrast and opened to a wide community: Spectro-Polarimetric High Contrast Exoplanet Research[7] (SPHERE) and Gemini Planet Imager[8] (GPI). While other techniques, qualified as "indirect," use stellar photons to

*Address all correspondence to: Jean-Francois Sauvage, E-mail: sauvage@onera.fr

2329-4124/2016/$25.00 © 2016 SPIE

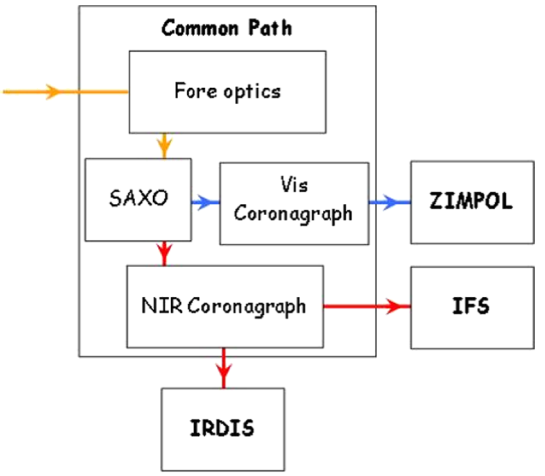

Fig. 1 Global concept of the SPHERE instrument, indicating the four subsystems and the main functionalities within the common path subsystem. Optical beams are indicated in red for NIR, blue for Vis, and orange for common path.

detect and characterize an orbiting planet, direct imaging used in these instruments consists in grabbing directly the photons from the planet. Such observation brings rich amounts of information allowing to fully characterize the properties of exoplanets, including indications of habitability, physics and chemistry of their atmosphere. The direct methods are therefore a unique means to retrieve crucial information for planetary science. Such extremely challenging scientific objectives directly translate into a relatively complex high-contrast instrument, combining coronagraphic techniques and dedicated imaging strategies. XAO is the core of ground-based high-contrast instruments, with the aim to compensate for the wavefront perturbations due to the imaging through the atmospheric turbulence. It also enables the self-correction of internal errors of the instrument.

The SPHERE system[9] aims at detecting extremely faint sources (giant extrasolar planets) in the vicinity of bright stars. The detection limit for the SPHERE instrument is 10^{-6} at 0.5 arc sec (i.e, 15 magnitudes between the star and the planet) with a goal around 10^{-7}. There is no direct link between the AO system performance and the final detectivity of the instrument; nevertheless, the impact of AO on the final performance is related to the performance of the coronagraph. A better AO correction leads to a better coronagraph extinction and therefore leads to the following improvements in system performance:[10]

- a reduction of the photon and flat-field noises [i.e., a gain in signal-to-noise ratio (SNR) for a given integration time]
- a reduction of the static speckle (through the reduction of airy pattern intensity due to the coronagraph optimization).

To meet the requirements in terms of detection,[11] the proposed design of SPHERE[9] is divided into four subsystems, namely, the common path optics and three science channels. The common path includes pupil-stabilizing fore-optics (tip/tilt and derotator) where insertable polarimetric half-wave plates are also provided, the SPHERE extreme adaptive optics (SAXO) system with a visible wavefront sensor (WFS), near-infrared (NIR) coronagraphic devices in order to feed the infrared dual-imaging spectrograph (IRDIS)[12] and the integral field spectrograph[13] with a highly stable coronagraphic image in the NIR. The SPHERE instrument also presents the unique opportunity of visible capabilities with the polarimetric imager ZIMPOL.[14] The three scientific channels gather complementary instrumentation to maximize the probability of exoplanet detection and to give access to a large range of wavelengths and information (e.g., imaging, spectra, and polarization).

The concept behind SPHERE is illustrated in Fig. 1, where the different handling of spectral bands is indicated: NIR-Vis is common to all instruments, the NIR path, and visible path. In order to fully characterize the instrument quality, two AIT periods have been mandatory. In the first phase at Observatoire de Paris, the performance of SAXO itself was assessed. In the second phase at IPAG Grenoble Observatory, the operation of SAXO in interaction with the overall instrument (Grenoble Observatory) has been optimized. In addition to the first two phases, a final check has been performed after the reintegration of the overall instrument at Paranal Observatory, in the New Integration Hall (NIH) before integration at the telescope focus. Images of Fig. 2 show the status of SAXO at each of the three different steps.

This article will be dedicated to the presentation of SAXO system performance and tests, assessed during these three periods. The following section is dedicated to the description of

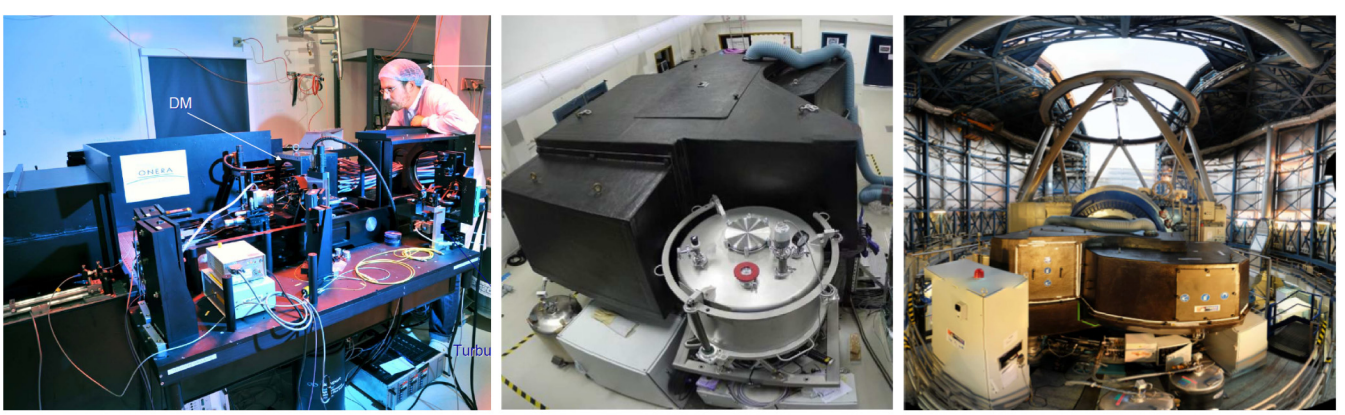

Fig. 2 (a) SAXO being tested at Meudon Observatory. (b) SPHERE in its final shape at IPAG (8 tons, 6-m length, 4-m large, 2.5-m height). (c) SPHERE at the UT3 telescope Nasmyth focus.

the AO system itself. A global overview will be shown, as well as requirements and implementation. We present the pure AO performance, as measured in laboratory, including a study of the limitations. Then, the system performance on turbulence phase screen will be demonstrated. Last, the coronagraphic performance will be demonstrated.

2 SAXO System Description

SAXO is the core of the SPHERE instrument and is essential for reaching the extremely high contrast requirements. In this framework, SAXO must fulfill the following three high-level requirements. First, it has to ensure the measurement and correction of the turbulent phase perturbations of the telescope and system common optics aberrations and of the noncommon path aberrations (NCPAs) (main AO loop). Second, it should ensure an extremely high stability (at low temporal frequency) of the optical axis at the level of the coronagraphic mask [using an infrared (IR) differential sensor as close as possible to the coronagraphic mask, the differential tip/tilt sensor (DTTS)]. Finally, it should ensure the measurement and the correction of any pupil motion [using a pupil motion sensor (PMS)].

2.1 *SAXO General Requirements*

SAXO high level requirements are directly extracted from the SPHERE technical specification and the SPHERE subsystem functional requirements. They are listed in Table 1. These values have driven the whole SAXO design.

The first and critical point to be addressed for any AO system optimization is the performance estimation parameter. The usual performance criterion for AO systems is the Strehl ratio (SR). This criterion quantifies the point-spread function (PSF) quality for noncoronagraphic systems. In the case of SPHERE, the final performance of the system is not a SR but a contrast value. However, we want to show here that there is a link between the SR and the coronagraphic extinction. During the past few years, a large number of coronagraphic devices have been proposed, ranging from modified Lyot concepts (with apodization for instance[15]) to interferometric devices, such as the four quadrants coronagraph.[16] Each approach has its own advantages and drawbacks. Many coronagraphic concepts have been proposed, based on opaque masks or phase masks. In any case, the purpose of the coronagraph is to remove the coherent light coming from the on-axis guide star (GS). Therefore, one can analytically define a "perfect coronagraph" using the following equations:

Table 1 Requirements for SAXO subsystem.

Specification	Value
Maximum residual tip/tilt in nominal conditions (0.85 arc sec seeing), for both axes cumulated	3 mas RMS
Maximum turbulent residual wavefront variance on corrected modes in normal conditions	60 nm RMS
Radius of AO-corrected field up to $\lambda/2d$ with d	0.2 m
SR (1.6 μm) in poor or faint conditions	>15%
Ability to stabilize pupil in translation: of pupil diameter	<0.2% (goal = 0.1%)
Ability to reproduce an image position and to stabilize the image in translation, (hence compensate image movements due to thermo-mechanical effects and differential atmospheric dispersion between Vis and NIR bands)	<0.5 mas (goal 0.2 mas)
The residual NCPA after phase diversity measurement and AO precompensation	<0.8 nm (goal 0.4 nm) per mode
Noncommon path defocus residual	<50 nm
NCPA residual on the 55 first Zernike modes	<55 nm RMS

$$C_{\text{res}}(\rho) = \left\langle \left| FT\left[P(r)A(r)e^{i\Phi_{\text{res}}(r)} - \sqrt{E_c}P(r)\right]\right|^2 \right\rangle,$$

where $C_{\text{res}}(\rho)$ corresponds to the image intensity in the focal plane after the coronagraphic process. ρ stands for the focal plane position, r for the pupil plane coordinates, $\langle . \rangle$ for a statistical average, $A(r)$ for the wavefront amplitude, $\Phi_{\text{res}}(r)$ for the residual phase after AO correction, $P(r)$ for the pupil function, and E_c for the short exposure coherent energy, which can be defined as follows:

$$E_c = e^{-[-\sigma_\Phi^2 - \sigma_{\log(A)}^2]}$$

with σ_Φ^2 and $\sigma_{\log(A)}^2$ being, respectively, the variance of phase and amplitude effect across the pupil.

According to Perrin et al.[17] and for small phase regime, it quickly comes that as a first approximation (first-order expansion), the coronagraphic image intensity is proportional to the residual phase power spectral density (PSD):

$$C_{\text{res}}(\rho) \propto \langle |FT[\Phi_{\text{res}}(r)]|^2 \rangle.$$

Based on this approximation of the image formation, the requirements can be clarified. The coronagraphic profile is proportional to the PSD of the phase, and the SR is $e^{-\int \text{DSP}_\Phi}$. The contribution of PSD to the final coronagraphic image can be separated according to the localization in the focal plane. For practical purpose, we separate the PSD contribution in three terms: first, the tip/tilt residual, which presents a strong impact close to optical axis, the PSD contribution to the corrected halo up to the cutoff frequency of AO, and then the PSD contribution outside of the AO corrected halo. The final SR can be rewritten as follows:

$$\text{SR}_{\text{Im}} = e^{-\sigma_{\text{TipTilt}}^2 - \sigma_{\text{Halo}}^2 - \sigma_{\text{Uncorrected}}^2}.$$

The contribution of uncorrected PSD is mainly due to atmospherical perturbation at high spatial frequency, out of sight of the XAO system and therefore uncompressible. From this analysis, we can see that the SR in the image is a good criterion for the behavior of SAXO and will be used in the following as the quality criterion of the subsystem. In addition as the contrast is the final criterion of the whole instrument, we will present at the end of the paper some raw contrast and differential contrast results in order to fully demonstrate the performance of SAXO.

2.2 *SAXO System Design*

The SAXO system (Fig. 3) is made up of three loops plus an offline calibration: the main AO loop compensates for

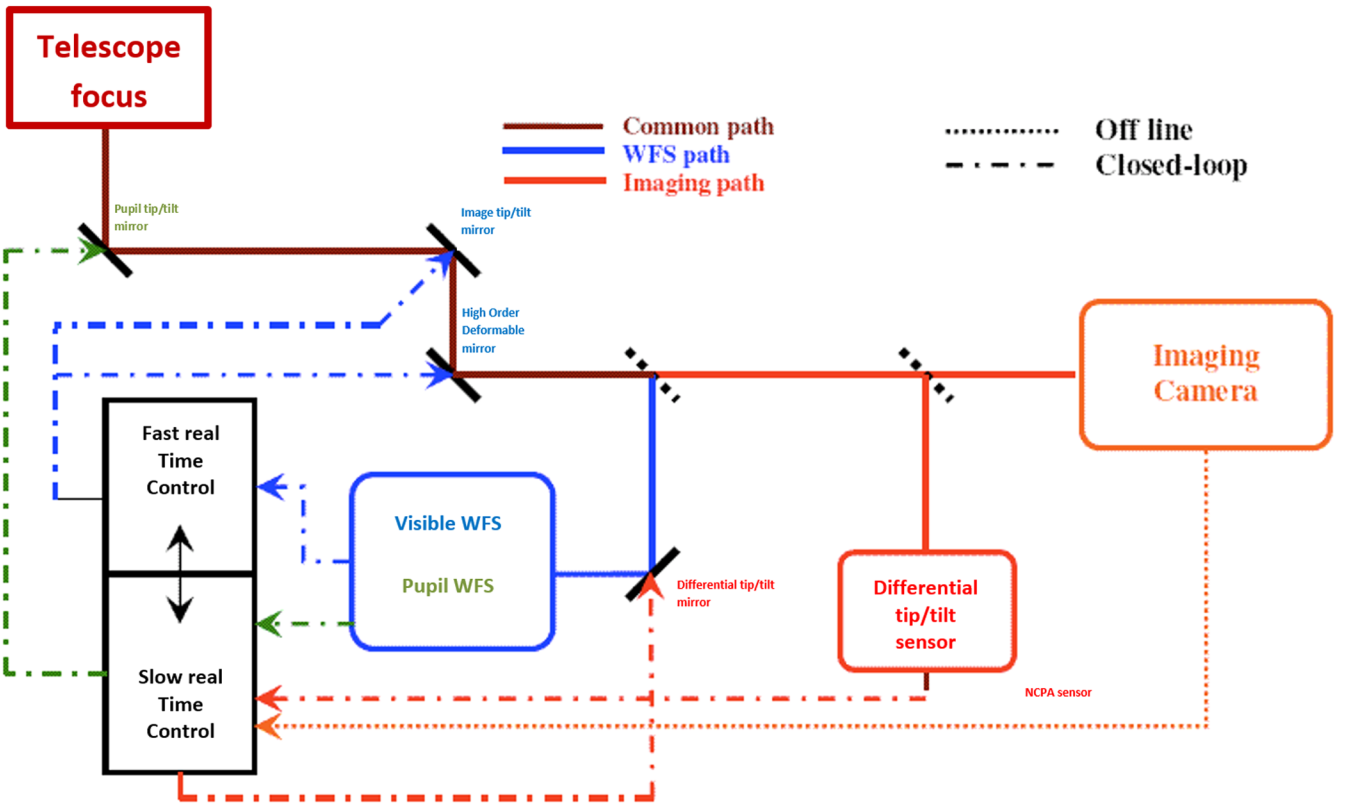

Fig. 3 Schematic representation of SAXO loops. The components of the fast turbulent loop (visible WFS, HODM and ITTM, fast RTC) are shown in blue and black, the components of slow loops (differential tip/tilt sensor in red, differential tip/tilt mirror, as well as pupil loop in green and NCPA sensor in orange), and the different retroactions indicated as solid, dotted, and dashed lines. Offline calibration refers to the NCPA measurement and compensation, see Sec. 3.3 for details.

atmospheric, telescope, and common path defects. The main impact is the increase of detection SNR through the reduction of the smooth PSF halo due to turbulence effects. The DTTS loop ensures a fine centering on the coronagraphic mask by correcting the differential tip/tilt between the VIS and NIR channels. It will ensure an optimal performance of the coronagraph device. The pupil loop compensates for pupil shift due to both telescope and instrument,[18] so that the uncorrected aberrations effects will remain at a fixed position in the focal plane. A post-processing procedure will be used to clean out these residuals. Finally, the NCPA's precompensation reduces the persistent speckles. In addition to these loops, the XAO system will also provide different features for the monitoring of the environment evolution:

- antiwind up and garbage collector loop[19] allowing to deal with saturated actuators;
- a tip/tilt and focus off-load process on telescope M2;
- a turbulence parameter and system performance online monitor.

The global performance of tip/tilt of the SAXO subsystem is decomposed into two main contributors: the turbulent tip/tilt correction and the absolute centering of star on coronagraph. Both contributors are the raw contrast image limitation and need particular care. The first contribution is described by the dedicated linear quadratic Gaussian (LQG) control law, whereas the second is described by the differential tip/tilt loop and is described in 3.5.1.

2.3 *Adaptive Optics Components*

SAXO is made of the following building blocks: active tip/tilt devices, sensors, a deformable mirror (DM), and a real-time computer (RTC).

2.3.1 *Active tip/tilt devices*

A fast image tip/tilt mirror (ITTM), provided by LESIA (Observatoire de Paris), is located in a pupil plane for image motion correction. It provides a phase lag of 13 and 11 deg, respectively, for X and Y axis instead of a required 5 deg but this excess does not represent a major issue in the system.

A slow pupil mirror, the PMS, is located close to the entrance focal plane to compensate for pupil shifts. Controlled using the flux measured in subapertures located at the edge of the pupil in a quad-cell-type arrangement, this system is able to stabilize the SPHERE pupil with accuracy largely better than the required 0.5% of the full pupil.

A spatial filter device[20,21] is added in front of the WFS to reduce the aliasing effects. It is a squared device with a variable size (from 0.7 to 2.1 arc sec). This component is compliant in terms of speed and accuracy of size variations as well as centering with respect to optical axis down to 30 mas on-sky.

The high-order deformable mirror (HODM) is provided by CILAS company and is described in Sec. 2.3.4.

2.3.2 *Sensors*

The 40×40 visible spatially filtered Shack–Hartmann (VIS-WFS) includes an EMCCD manufactured by E2V company with 240×240 pixels (pixel size is 24×24 μm). The WFS camera was developed by ESO and the final version, delivered in July 2013, fulfills and even shows exquisite results in terms of noise ($<0.1e^-$), read-out speed (>1200 Hz), quantum efficiency, and pixel transfer function. In particular, these values contribute to the high performance of the system in terms of limiting magnitude (see Sec. 3.5.3). An illustration of the WFS signal can be seen on Fig. 4, with the 40×40 subapertures, and the very large telescope (VLT) pupil geometry with 14% obscuration as well as the 5-cm-thick spiders' arms.

A slow IR DTTS[22] is included in the scientific channel close to the coronagraph plane to measure the relative image motion between the WFS and the coronagraph. The DTTS loop characteristics fulfills the specification in term of measurement accuracy and loop bandwidth and the final accuracy in terms of optical axis stabilization is lower than 0.5 mas, which is well within the specifications.

2.3.3 *Real-time computer and algorithms*

The RTC, named SPARTA,[23,24] is provided by ESO. SPARTA offers, as specified, a very modular and fine-grained RTC architecture. It includes the definitions of all the interfaces between the SPARTA modules and provides libraries and tools for their implementation and testing, as well as a mapping of technologies capable of delivering the required performance. These comprise, among others, VXS communication (VMEBus Switched Serial), field-programmable gate array aided wavefront processing, command time filtering, digital signal processing-based wavefront reconstruction, data distribution service, and multi-central processing unit number crunching. In particular, the RTC includes a mixed control law: an optimized modal gain integrator[25] for the DM control and a LQG for the tip/tilt mirror LQG control. The LQG description can be found in Petit et al.[26]

The LQG control law is an optimal control approach first introduced in AO by Paschall and Anderson.[27] This optimal law, coupled with an automatic process of identification of turbulence vibration and measurement noise, controls the tip/tilt mirror of SAXO in charge of the correction of the atmospheric turbulent tip/tilt aberrations. As the vibration identification and optimal compensation is mandatory in a telescope environment, especially when dealing with such level of performance, the filtering of vibrations proposed by Petit et al.[28] and the identification process proposed by Meimon et al.[29] have been implemented in SAXO control laws. The vibration peaks are modeled based on pseudo-open loop data by AR2 filters, as shown in Fig. 5. Up to 10 peaks can be identified on each axis between 20 and 200 Hz, and the corresponding control law is modified to optimally extinct them as fast as the system frame rate can. This is the first autotuned LQG-based control on an operational system. The LQG models and control law are thus regularly updated on a 2-min time basis.

A weighted center of gravity algorithm[30] is used for slope estimations.

A phase diversity algorithm[31] was implemented to measure the NCPA between the WFS and the coronagraph allowing their compensation by setting appropriate reference slopes. The algorithm has been successfully implemented in the instrument software and the residual NCPAs after the iterative compensation process show impressive performance: the measured SR is larger than 99% in H band, which means <20 nm RMS of residuals and <5 nm on the 50 first modes.

2.3.4 *Deformable Mirror*

A fast HODM is used to correct for any phase perturbations but the tip/tilt. With flatness of <1 μm mechanical peak-to-valley, and no dead actuators at the moment of delivery, this mirror, capable of delivering 12-μm mechanical peak-to-valley actuator stroke, is the main building block of the SPHERE instrument.

The specifications for HODM are listed here:

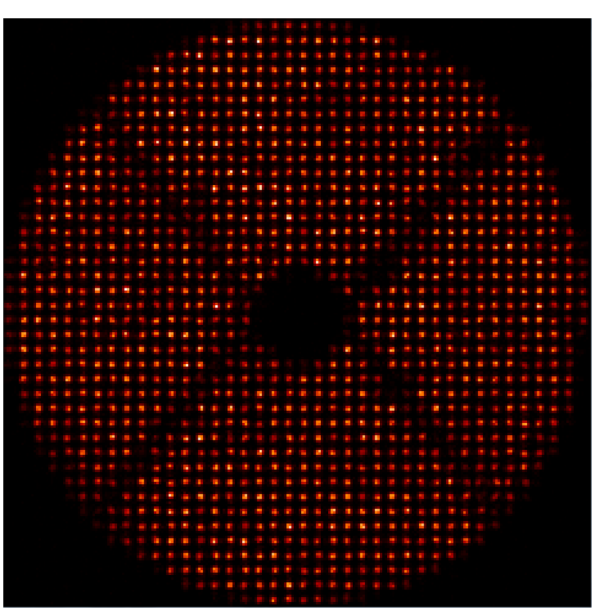

Fig. 4 Illustration of visible WFS spots, as seen by the WFS detector on internal calibration source after background subtraction. The image is acquired in closed loop on laboratory turbulence introduced by the AIT turbulence simulator.

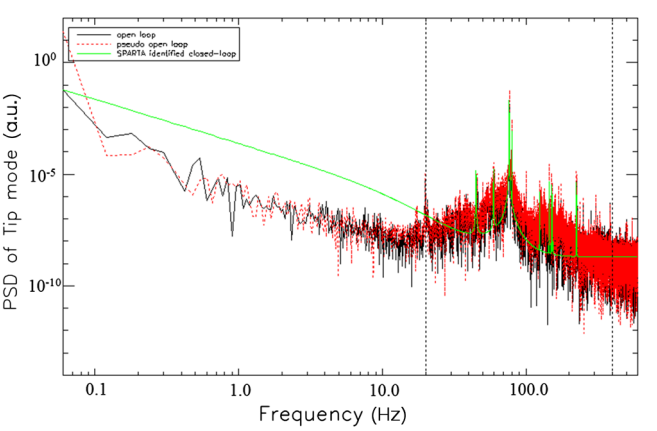

Fig. 5 Example of identification run on pseudo-open loop data: the temporal PSD of first tip axis (corresponding to horizontal axis physically on the bench) are fitted with 10 different autoregressive second-order filters for vibration peaks,[33] and one for turbulence.

- 41×41 actuators with a rectangular pitch (4.5 and 4.51 mm) to match SPHERE optical design. The pitch is different in X and Y axis due to the incident angle of 4 deg on HODM;
- 1.5 μm of mechanical interactuator stroke, this value is the maximal differential mechanical deformation that can be reached between two neighbor actuators;
- 10-μm mechanical stroke, this value is the maximum deformation reachable by the DM on large scale;
- a shape at rest lower than 1 μm, this value is the natural deformation of the DM, that is we wish to be small enough to leave the maximum deformation to the turbulence correction;
- no dead actuator (and in particular no stuck actuator);
- high temporal response: bandwidth at 0 dB attenuation higher than 1 kHz with neither mechanical nor electronical resonance below 5 kHz for all the actuators;
- operation conditions: up to 99% of humidity and between 5 and 15 deg (usual Paranal temperature range).

A special attention has been brought to the handling of the 69 actuators close to the edge of the pupil (external edge of primary mirror or central occultation of secondary mirror). These actuators are controlled by subapertures partially enlightened, hence providing a signal more noisy than the other subapartures. In order to avoid any divergence, or wrong behavior of these actuators, they are declared as slaved in the control loop. It means that they are not controlled in real time (their voltage remains constant during closed-loop process). For these actuators, their static contribution is computed from the static value of their closest neighbors, which is calibrated daily.

During the life time of the project, we faced a major issue due to the ageing of the HODM. The number of dead actuators now reaches 18 and the HODM shape at rest has changed, and evolves with temperature, so that it can reach more than 100% of the full mirror stroke.

We propose to focus now on the HODM issues met during SAXO AIT and on the mitigations procedures proposed by the consortium. Although the system performance is barely affected by the current bandwidth limitation, the shape at rest (and especially its evolution with temperature) and the DM dead actuators represent the most severe limitations and medium-to-long term risks of the SPHERE system.

Dead actuator mitigation. We define three different types of dead actuators: the ones with short circuit, the ones with contact issues (between wires and piezo material) and the ones with extremely slow response (i.e., a very high resistance). The number of dead actuators has grown from 2 to 18 in 4 years and this increase appeared to be due to the high hydrometry in the integration rooms. An active dry system has therefore been installed into the HODM itself to mitigate the impact of humidity on the actuators. Since the installation of HODM at Paranal (12 months), there was no new dead actuators. Considering the HODM design, any operation on these actuators is almost impossible and thus, this defect cannot be fixed. It has been demonstrated (both in simulation and in labs) that the impact on performance of such a number of dead actuators (stuck to a position corresponding to zero voltage) is the main contributor to the contrast loss. Adopting a strategy proposed by the GPI team,[32] modified Lyot stops (occulting the pupil area containing the dead actuators have been manufactured for each coronagraph (both in IR and VIS) and installed in SPHERE. Figures 6(a) and 6(b) show the pupil image downstream of the coronagraph. On left side, the impact of dead actuators is clearly visible, each dead actuator resulting in a residual bright peak located at the position of the actuator. The gain in performance is demonstrated in Figs. 6(c) and 6(d). The effect of the dead actuators in the coronagraphic PSF (left) results in bright structures corresponding to interference pattern due to residual bright peaks. By masking the peaks, these patterns are efficiently blocked. With the custom Lyot stop, the performance is nearly perfect even with an extra dead actuator that was not there are the times of the Lyot stop mask design. In addition, all HODM dead actuators are devalidated in the RTC system, so as to minimize their impact in the closed-loop process.

Shape at rest mitigation. Since the manufacturing and acceptance of the HODM, two main problems appeared. First, due to an ageing effect, the global form of the optical surface is warped cylindrically and the amplitude of the bending is about half the stroke of the actuators. This effect means that the flattening of the HODM requires a lot of dynamic, which will not be used for the correction of the atmospheric turbulence. Even if some explanations have been proposed to this effect, no real solution has been found. Second, the form of the HODM evolves with the temperature (Both problems are illustrated on Fig. 7). This effect is extremely important and leads to a bending of 1 μm/K. Some experiments have been done on the XAO characterization bench and shown that the form error is equal to the full stroke of the actuators at $T = 296$ K. Considering that the HODM must run between 278 and 293 K, this effect is clearly not acceptable and needs to be compensated for. To compensate for these effects, we use one of the toroidal mirrors (TM3) whose mechanical shape has been optimized for astigmatic and cylindrical bending for the stress polishing phases.[34,35] TM3 is the only mirror capable to be bent up to 20 μm of cylinder without any breakage risk and is therefore chosen to be the compensating mirror. The optical performance of such a correction, done on a mirror outside the pupil, has been estimated using ray-tracing software. The results demonstrate that a perfect correction will not impact the image formation. The resulting pupil ellipticity is equal to 0.5%, fully in the specifications of the instrument. A specific warping harness has been designed, realized, and attached to the back of the mirror's substrate (as illustrated on Fig. 8), which optimized shape allows the use of a single actuator to obtain the right shape as well as an optimal resolution of the bending. This kind of "woofer-tweeter" configuration gives a preliminary flattening of the wavefront of about 1 μm PtV in the nominal case, 2 μm PtV in the most demanding case. The XAO system then recovers its correction capabilities, with about 10% of the stroke used for the fine flattening of the wavefront, the rest being used for turbulence correction. Although the DM is not perfect yet, the current version allows a full SPHERE operation and does not significantly degrades the performance, its potential degradation remains a real concern for the project and one of the most important risk for the whole SPHERE mission. CILAS, together with ESO and TMT, are currently working on a recovery plan to improve their manufacturing processes in order to have, in the future, a viable solution for the next DM generation.

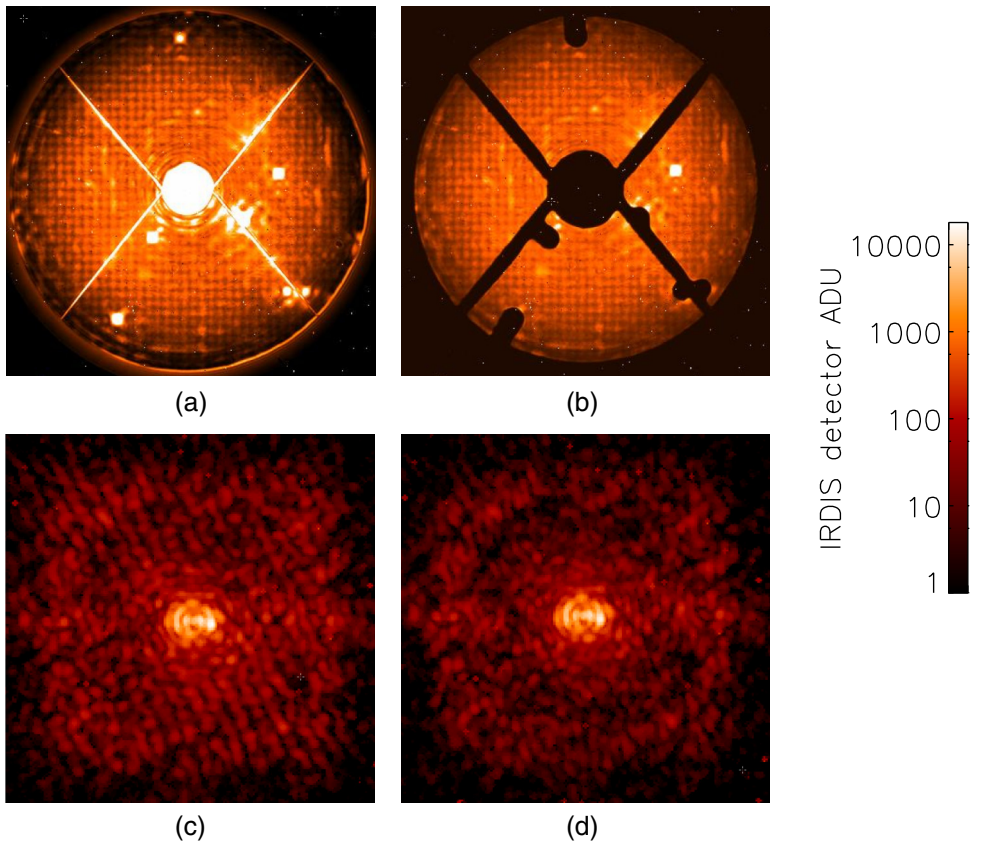

Fig. 6 (a and b) Raw coronagraphic image of pupil plane and (c and d) focal plane, (a and c) without masking the dead actuators, (b and d) with masking the dead actuators. 18 dead actuators are present on the DM at the date of this image. Only eight are easily visible in this image. Six others are situated close to the right edge of the pupil, three have no impact due to their natural dead position, being close to the ideal flattening shape of the DM. It is to be noted that the modified Lyot mask has been designed only for 17 dead actuators; hence, the bright spot visible on the right image, on the right side of the pupil. The 18th dead actuator was declared dead after the Lyot stop manufacturing. Hopefully, the impact of one single dead actuator is not a major issue to the final performance.

2.4 *System Operation*

2.4.1 *Loop closure strategy*

As described in the previous sections, the SAXO system includes several control loops working at different time scales. The loop closure strategy refers to the sequence of operations to be performed when closing the loops. This strategy has been set up in laboratory and will further be refined during on-sky commissioning of the instrument. The tip/tilt loop is closed first, recentering the spots in the subapertures and strongly reducing

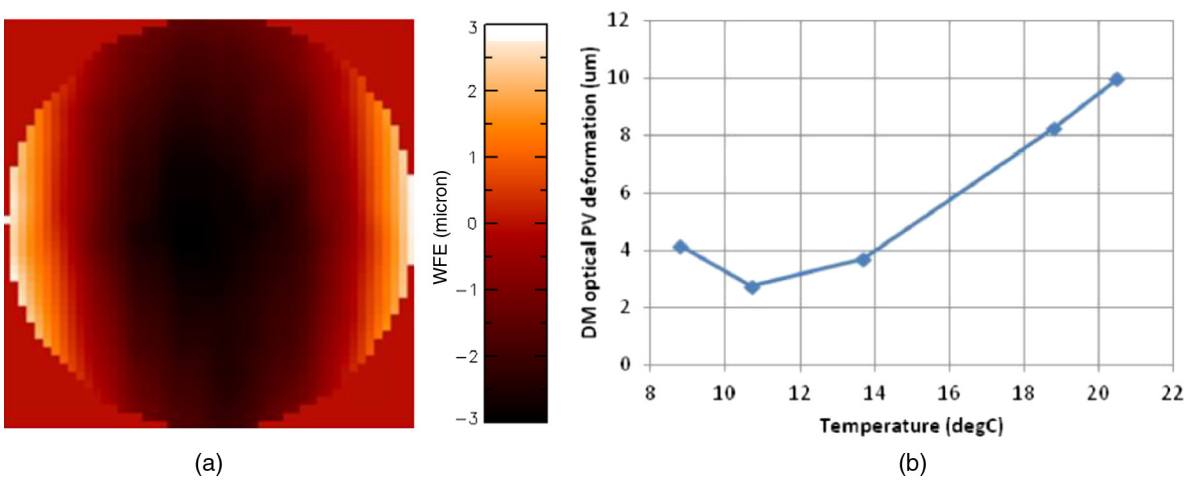

Fig. 7 (a) DM typical shape at rest, for a temperature of 16.5 deg. (b) Evolution of the shape at rest with temperature.

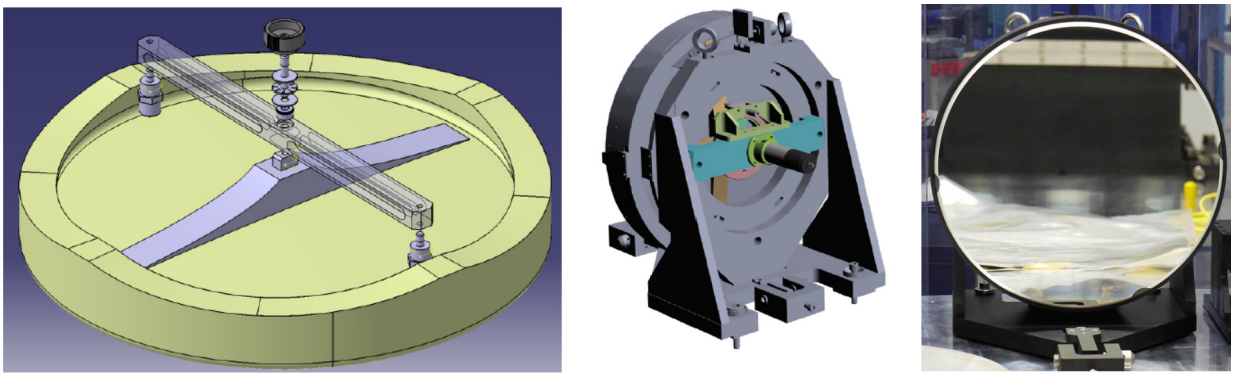

(a) (b) (c)

Fig. 8 (a) Model of active toric mirror 3 (ATM3) modification with one actuator situated on the rear side of the mirror, dedicated to HODM cylinder compensation. (b) 3-D model of constraint mechanism with motorization and the complete mount, and (c) picture of the face view of toric mirror 3.

the phase residual on the WFS. The HODM loop is closed after the first loop convergence and gives the main contribution to performance by gathering all light in a coherent peak. The pupil loop is closed to keep the pupil centered on the WFS. Finally, the differential tip/tilt loop can then be closed, using the PSF corrected by the first two loops, to center the PSF on the coronagraph during the whole observation. During the lab integrations, each step of these three loops is followed by quality checks on the system behavior. The residual slopes after correction are the witness of a healthy system and are used to compute quality criterion.

2.4.2 *Interaction matrices acquisition*

Each of the SAXO loops requires the acquisition of an interaction matrix. The interaction matrix refers to the link between the sensor and the corrector. A brief description of these interaction matrices is detailed here for each of them. The fast tip/tilt interaction matrix is calibrated by actuating each axis several times and recording the sensor slopes modification. The recording needs a few seconds only. The HODM interaction matrix represents a large number of actuators and slopes' measurement. It is calibrated due to a dedicated Hadamard process.[36] This process allows to decrease the calibration time, keeping the SNR of interaction matrix high. The calibration time is a few minutes (typically 5 min). The differential tip/tilt loop needs a dedicated calibration matrix. This matrix is calibrated by actuating each axis of the differential loop several times, during closed loop on fast tip/tilt and HODM loops. The pupil loop interaction matrix has to be calibrated on-sky, as there is no materialization of the pupil upstream of the pupil mirror of SAXO. It is calibrated by actuating each of the axes of the pupil loop several times, while recording the PMS. It is to be noted that the pupil mirror is situated upstream of the beam derotator. The pupil image on the WFS is therefore rotating with respect to the pupil image on the pupil mirror. The interaction matrix of pupil loop has to be rotated every time the derotator has been rotated by more than 1 deg during operation, in order to ensure a correct control of the pupil mirror.

3 Performance Tests

We will focus now on the performance tests done to ensure that SAXO reaches its nominal performance. We will first describe the tools (turbulence simulator) and performance criterion for the tests, and then go deeply into the test results analysis.

3.1 *Turbulence Simulator*

In order to quantify the performance correctly, a dedicated module of turbulence generation has been used. This module called TSIM (see Fig. 9) for turbulence simulator uses reflective phase screen plates produced by SILIOS company. After one reflection on the plate, the optical beam reproduces the atmospheric turbulence. Two rotating plates are foreseen in the TSIM to receive phase screens. Two turbulent phase screens can be used either one at a time (the other one being a flat screen), or simultaneously (the turbulence effect therefore accumulates). Due to the two phase screens of Fried parameters at 0.5 μm $r_0 =$ 12 cm (low-level turbulence) and $r_0 = 16$ cm (nominal turbulence), the turbulence strength that can be produced is

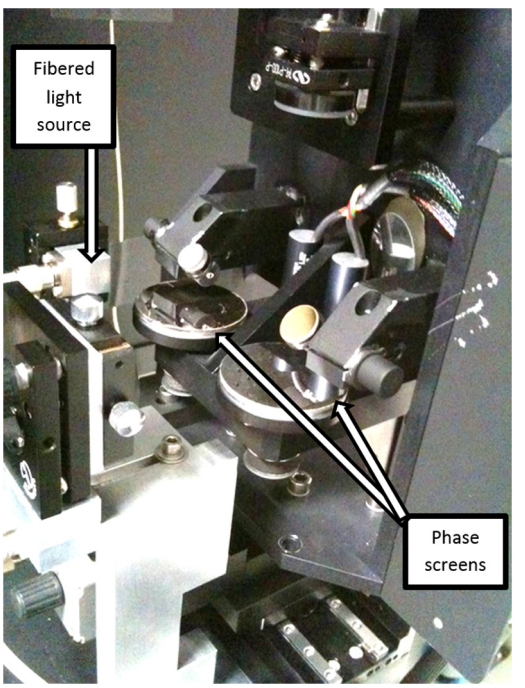

Fig. 9 Simulation of turbulence for SPHERE. The heart of TSIM: two rotating reflective phase screens.

$\theta_0 = 0.64$ arc sec, $\theta_0 = 0.84$ arc sec, and $\theta_0 = 1.12$ arc sec by combining the two phase screens.

The phase screens are calibrated by different means.

- An external calibration is performed on a dedicated bench and using a 128×128 industrial WFS HASO™. This calibration allows estimation of the strength of the phase screen itself. The variance averaged on each Zernike radial order shows the expected shape for the high orders (see Fig. 10). The first radial order, corresponding to tip-tilt (TT), is affected by the wobble of the rotating mount. Even if this wobble has been minimized by tuning the orientation of the mount, the variance for low radial orders has not been taken into account in the fit. The strength of the two phase screens is estimated at $\theta_0 = 0.62$ arc sec and $\theta_0 = 0.81$ arc sec by this mean.
- Uncorrected long exposure images are acquired with the instrument itself. The light distribution in such images (see Fig. 11) gives a precise estimation of the strength of the turbulence: the full-width at half-maximum of the spot is related to the turbulence strength.
- The RTC SPARTA provides regular statistical estimation of the turbulence parameters, including Fried parameter and wind speed. This estimation relies on the computation of pseudo-open loop turbulent modes from closed loop residual slopes and closed loop correction voltages. As detailed in Fusco et al.,[37] the turbulence parameters are estimated from the pseudo-open loop data due to analytical behavior. The precise estimation of the noise variance is the key point to access to turbulence parameters. This spurious parameter is estimated in the temporal autocorrelation of pseudo-open loop data.

The measurements given by these different methods are compared in Sec. 2, and show a good concordance to the original specification of the phase screens, ensuring a performance test in realistic conditions.

3.2 *Performance Criteria, Computation Processes and Accuracies*

The performance of SAXO is expressed in SR. This quantity characterizes the optical quality of the imaging system. It is based on an analysis of the PSF of the optical system. This

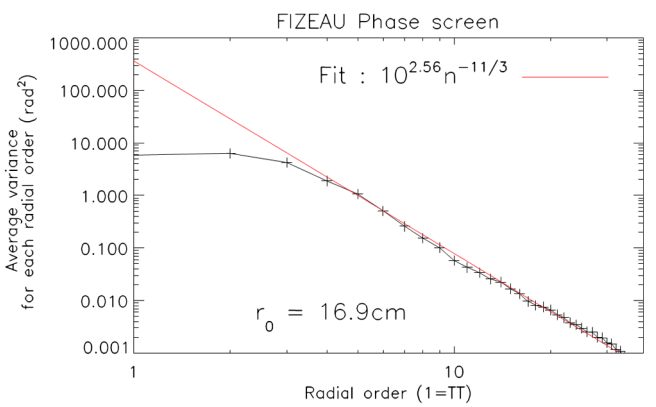

Fig. 10 Calibration of the phase screen $r_0 = 168$ mm by HASO: the Fried parameter fits to the expectation.

function represents the light distribution in the focal plane of a point light source positioned on the optical axis, with a flux normalized to one photon. The ideal light distribution is called unaberrated PSF i_{NoAb}. The real-light distribution of the optical system is i_{Ab}, which differs from the ideal distribution due to phase and amplitude aberrations present in the optical system, degrading the image quality.

As defined in Mahajan,[38] the SR corresponds to the ratio between the on-axis value of the PSF $i_{\mathrm{Ab}}(\vec{0})$ on the on-axis value of the unaberrated PSF $i_{\mathrm{NoAb}}(\vec{0})$. The SR value can be computed using the following Eq. (1):

$$\mathrm{SR}_{\mathrm{im}} = \frac{i_{\mathrm{Ab}}(\vec{0})}{i_{\mathrm{NoAb}}(\vec{0})} = \frac{\int \tilde{i}_{\mathrm{Ab}}(\vec{f})}{\int \tilde{i}_{\mathrm{NoAb}}(\vec{f})}, \tag{1}$$

where $i_{\mathrm{Ab}}(\vec{0})$ and $i_{\mathrm{NoAb}}(\vec{0})$ are the on-axis values of, respectively, aberrated and nonaberrated PSF. From the definition of optical transfer function (OTF), it is equivalent to compute the SR in Fourier space, where $\tilde{i}_{\mathrm{Ab}}(\vec{f})$ and $\tilde{i}_{\mathrm{NoAb}}(\vec{f})$ are the OTF of the aberrated system and of the aberration-free system, and $\vec{f}$ is a position variable in Fourier space. The advantages of using the Fourier-domain definition for SR computation are manifold:

- As it is computed as an integral on whole of the Fourier domain, it uses all the pixels in the image, instead of using only the single on-axis pixel value;
- it allows an easy identification of residual background (null frequency residual) and of noise contribution (which can be identified at frequencies higher than the optical cutoff frequency);
- it allows an easy correction of both pixel and object transfer functions, see dotted line in Fig. 11.

Several parameters have to be taken into account in order to obtain accurate and unbiased estimation of SR: the pupil shape and potential apodization, the residual background, the noise in the image, the CCD pixel scale, and the size of the calibration source. Basically, all the parameters that are not due to phase aberrations have to be accounted for in the model of ideal PSF.

Figure 12 shows the OTF profiles in the case of an experimental data processing. The unaberrated profile (named "ideal profile" dashed-dotted line) accounts for the exact pupil shape and apodization functions. The SR is the ratio between the optical system OTF after correction (solid line) and the ideal OTF (dashed dotted line).

3.3 *Static Ultimate Performance, Internal Source*

Let us first consider the ultimate performance of the SPHERE system itself. The ultimate performance of the SPHERE system is ensured by correcting all the static phase aberrations internal to the instrument.

The precompensation of NCPA follows a procedure[39] of calibration based on a focal-plane measurement in the science focal plane, and a compensation by a modification of the reference slopes of XAO system. The reference slopes offset are modified and make compensation possible by SAXO closed loop.

The procedure of precompensation is performed once a day, during the whole instrument calibration phase. The modified reference slopes are stored and are planned to be used during

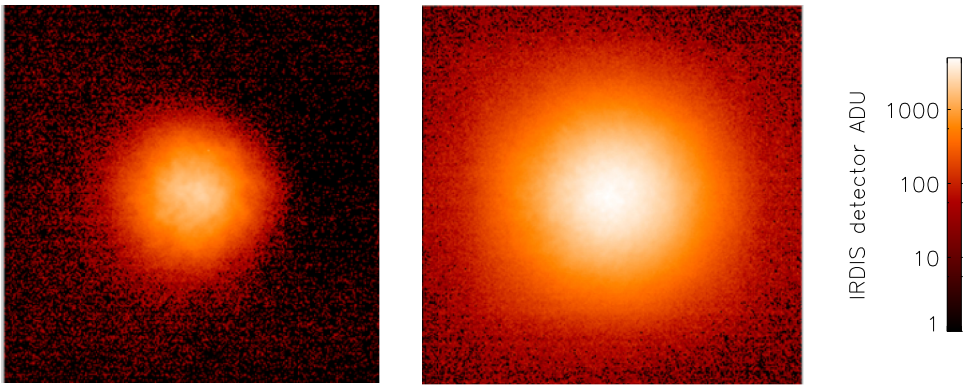

Fig. 11 Long-turbulent exposure (open-loop) obtained with IR imager. (a) Phase screen 0.85 arc sec. (b) Phase screen 1.12 arc sec. The FWHM of these spots is used to check the phase screens turbulence introduced by the turbulence simulator and given in Table 2.

every observation of the night. The stability of the NCPA has been characterized during integration at Grenoble[40] and showed an evolution in time that could be neglected during the nighttime.

The reference slopes of the SAXO system combine different measurements. The final value of reference slopes, used during SAXO AIT phase, is computed from the summation of 2.5 pixels (center of the subaperture), with additional contribution of the reference slopes calibrated on the reference path only ($\mathcal{S}_{\mathrm{WFS}}$, measured with a calibration source at the entrance of the analysis path) and of the NCPA contribution, calibrated in closed loop on the intermediate slopes $\mathcal{S}_{\mathrm{REF}} = 2.5 + \mathcal{S}_{\mathrm{WFS}}$.

The final reference slopes, including both WFS path and NCPA contribution, are computed due to the following Eq. (2):

$$\mathcal{S}_{\mathrm{REF}} = 2.5 + \mathcal{S}_{\mathrm{WFS}} + \mathcal{S}_{\mathrm{NCPA}}, \tag{2}$$

It is to be noted that there are many moving optical elements on the WFS path. The beam splitter sharing the light between ZIMPOL and the visible WFS can use three different elements, whose optical contribution differs from one to another. The spectral filters in front of WFS itself can use two different positions (completely open, or red filters). The ADC is moving with respect to the beam orientation and with respect to the zenithal angle.

Each of these moving elements modifies the optical aberration and therefore modifies the reference slopes. Thus, a set of reference slopes is calibrated for each of the element position, and recomputed with respect to the system configuration. It is to be noted that the ADC movement is a neglectible element due to the excellent optical quality of this device, <10 nm RMS for each prism, and is therefore not accounted for in this calibration.

Applying the reference slope modification as described below, Fig. 13 shows the final PSF quality, as measured in H band of SPHERE instrument with IRDIS instrument. The two images have been acquired using internal calibration source of the instrument, in closed-loop (hence without any turbulence, except for the local weak turbulence of the bench itself). Figure 13(a) shows the PSF obtained with the WFS path reference slopes. Figure 13(b) shows the PSF obtained when adding a correction term in the reference slopes, corresponding to the NCPAs. Table 3 gives the SR corresponding to the images of Fig. 13.

The final result shows a residual RMS value for the NCPAs (over all the phase spatial frequencies) around 25-nm RMS. The low orders of NCPA are compensated for. Even if the algorithm measures the aberrations as a phase map (described on 64×64 pixels), an equivalent of 20 to 50 Zernike polynomials has been compensated for.

Table 2 Cross-check of Fried parameter estimators.

r_0 (mm)	PS1	PS2
Specification	160	120
Calibration	168	126
Long exposure	167	124
SPARTA	154	118

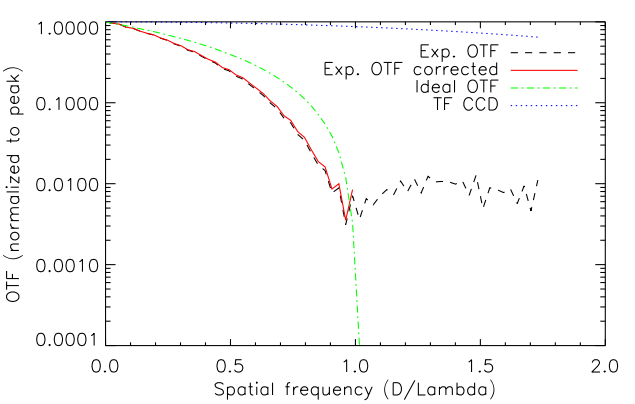

Fig. 12 SR computation in Fourier space. The OTF profiles are plotted here, in the case of an experimental image of SPHERE, with apodized pupil and Lyot stop. The quality of the PSF chosen for this example is bad (around 80% SR H band) in order to show the difference between the ideal profile (dash-dot) and the experimental profile (solid line).

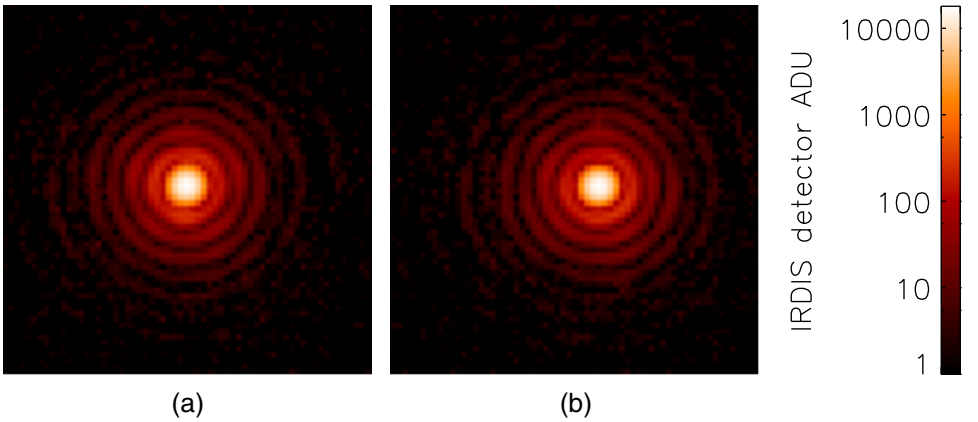

Fig. 13 Internal PSF of SPHERE instrument, obtained in closed-loop on the entrance calibration source. (a) PSF obtained with WFS path reference slopes. (b) PSF obtained with WFS path and NCPA reference slopes.

Table 3 Internal performance of the SAXO system, with respect to the choice of reference slopes computation. The NCPA compensation, at the date of the test, was producing a gain of 1.5% of Strehl ratio performance (H band).

Ref slopes	WFS path only	WFS path NCPAs
SR at H (%)	97.5 ± 1	99.0 ± 1
RMS (nm)	41 ± 10	25 ± 10

3.4 *Adaptive Optics System Temporal Behavior*

Rejection transfer function (RTF) is a simple and efficient criterion to quantify the overall system temporal performance. It translates the attenuation of the turbulent signal by the AO system and is here defined as the ratio between the residual phase spectrum $\mathrm{PSD}_{\mathrm{residual}}$ and the incident turbulent phase spectrum assuming high SNR (pseudo-open loop data $\mathrm{PSD}_{\mathrm{turbulent}}$), each depending on the temporal frequency f. The pseudo-open loop data are computed from the closed-loop voltage and the residual closed-loop slopes. Real open-loop data would not be accurate, as the strength of the uncorrected turbulence would drive the WFS out of its linearity domain. The phases are described as their decomposition on the DM or tip/tilt basis (voltage basis), and each actuator (1377 for the DM, 2 for the TT) are considered independent. The PSD is therefore obtained by averaging the voltage information on all the actuators. It is to be noted that the result has been validated also for each actuator independently so as to detect potential bad behavior actuator:

$$\mathrm{RTF} = \frac{\mathrm{PSD}_{\mathrm{residual}}(f)}{\mathrm{PSD}_{\mathrm{Turbulent}}(f)}.$$

In Figs. 14 and 15, the experimental RTF for HODM and ITTM is compared to theoretical expressions assuming a standard integrator controller with various gains. The sampling frequency is 1200 Hz and an excellent match is found on all RTF at all gain values for a 2.14 frames delay. This 2.14 frames delay includes the integration time, the readout time, and the RTC computation delay. This value is completely within the specification and very close to the goals. Note that the RTC pure delay has been

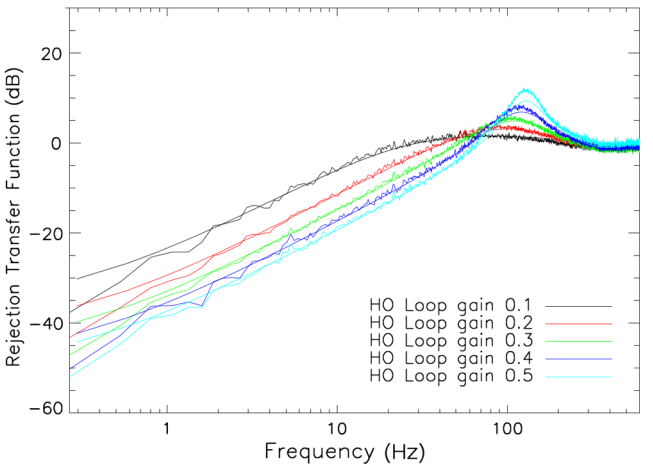

Fig. 14 HODM loop RTF as measured in laboratory on turbulent phase screens, for gain values (0.1 cyan, 0.2 blue, 0.3 green, 0.4 red, and 0.5 black), and theoretical fit.

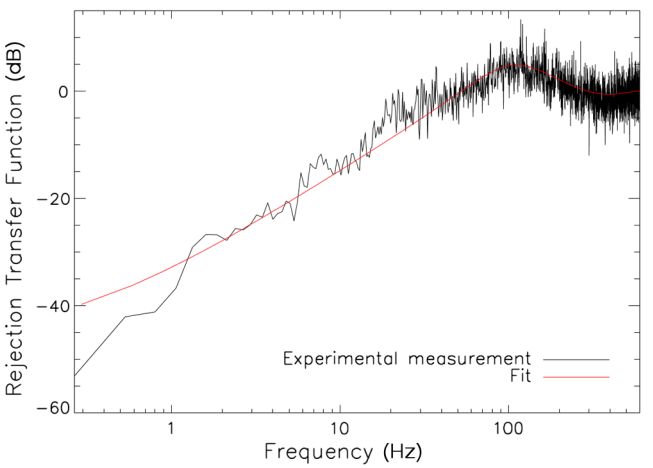

Fig. 15 ITTM loop RTF, as measured in laboratory on turbulent phase screens with a gain 0.3 and a simulated fit RTF with 2.14 frames delay.

measured separately and is equal to 80 μs (which is better than the goal of 100 μs), and demonstrates the high quality of the SPARTA system. All these numbers lead to a final system bandwidth around 70 Hz (measured at 0 dB for an AO loop gain of 0.5). This latency includes several contributions. Among them, one can cite

- wavefront processing: <2 μs,
- wavefront reconstruction: 40.5 μs, and
- wavefront control: 34.06 μs.

A more detailed description can be found in Suárez Valles et al.[24] In addition to classical integrator, an LQG control law has been implemented for tip/tilt mirror control in order to be able to deal with system and telescope vibrations and to ensure the smallest possible residual jitter. The LQG, also known as Kalman filter, and its associated online identification processes are detailed in Sec. 2.2.

3.5 *Adaptive Optics System Performance with Turbulence*

The performance of AO system has been assessed on turbulence during extensive test period at Meudon Observatory (2011 to 2012), at Grenoble Observatory (2012 to 2013), and finally at Paranal Observatory during the SPHERE integration on the telescope. The following subsections present the TT performance, the performance in nominal conditions, the performance for faint GSs, and the performance in poor turbulence conditions.

3.5.1 *Tip-tilt performance*

We focus here on the ultimate LQG performance. In Figs. 16 and 17, we compare (in terms of PSD and cumulative PSD) the temporal spectrum of the residual tip/tilt obtained with a classical integrator (gain = 0.5) and an LQG process (with online identification of turbulence and vibration peaks). The LQG law clearly shows a residual on the tilt of an order of magnitude lower (1/16th) than with the integrator law (visible on the last point at 600 Hz on the cumulated PSD). The residual tilt RMS with LQG is therefore 1/4th of the residual tilt RMS with integrator law. The main contribution of this is clearly visible on the two vibration peaks extinction at 45 and 70 Hz.

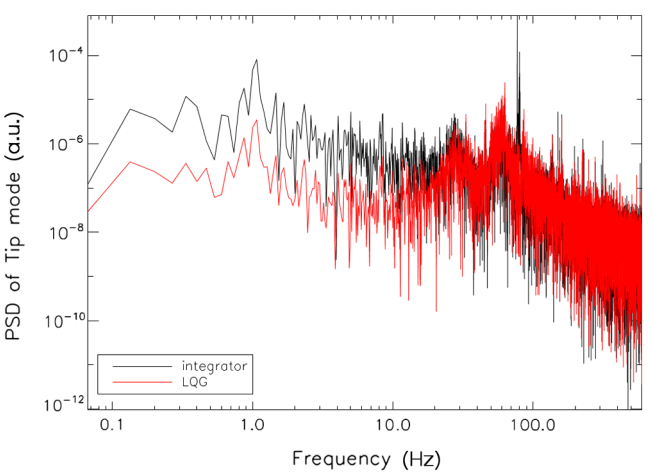

Fig. 16 Temporal PSD of first tip mode (corresponding to horizontal axis on the bench), with classical integrator (black curve) and LQG control law (red curve).

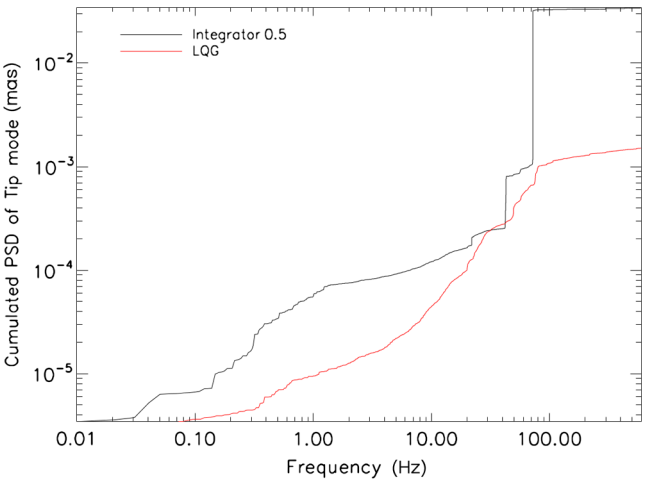

Fig. 17 Cumulated curves of PSD of previous Fig. 16. The *Y* axis unit is in mas on-sky. This graph therefore gives for each frequency *f*, the cumulated residual jitter in closed loop, for frequency range [0 – *f*]. Strong steps in black curve represent the impact of narrow band vibrations. The two control laws integrator (with gain 0.5) and LQG are compared.

In addition, when dealing with a coronagraphic system, the absolute pointing precision of the PSF onto the optical axis is a crucial point. The absolute pointing precision after AO correction should be better than 0.5 mas, to reproduce the PSF position in the focal plane with an accuracy better than 0.5 mas. To validate this important stability requirement, we have studied the reproducibility of the PSF position while repeating the following sequence:

- open all loops (Vis + IR)
- rotate IR ADC by 10 deg
- close all loops (Vis + IR)
- measure noncorono PSF position on IRDIS, with center of gravity algorithm

In order to introduce a change in the optical configuration and to validate the reproducibility of the centering, the SPHERE IR ADC prisms are rotated jointly, thus introducing a beam deviation (but no dispersion). Figure 18 shows the final positions of the PSF on science detector, after AO (turbulence and differential tip/tilt) correction. The maximum deviation to the reference position is equal to 0.35 mas, hence validating the high precision requested.

3.5.2 *Performance in nominal conditions*

The SAXO nominal performance is defined for the following conditions:

- *V* magnitude is around 9, i.e., 100 photoelectrons per subaperture and per frame on the WFS (at 1200 Hz)
- Seeing = 0.85 arc sec and wind speed = 12.5 m/s

In these conditions, with a fully operational and optimized SAXO system (all loops closed, all optimization processes including LQG vibration filtering on tip/tilt), we have recorded classical PSFs and coronagraphic images on IRDIS in dual-band

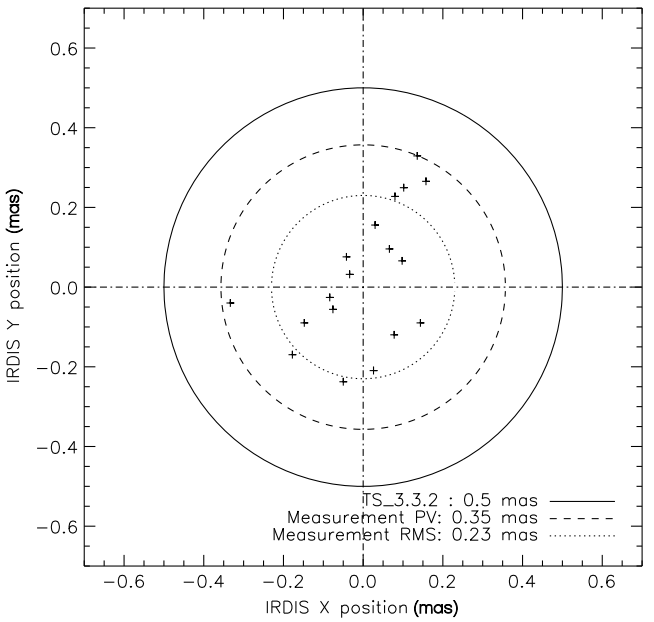

Fig. 18 DTTS absolute precision: position of PSF on IRDIS for different positions of the IR ADC. Moving the ADC was the only way to introduce some differential tip/tilt on the SAXO bench during AIT period (no simulation of atmospheric deviation was possible).

imaging mode,[41] as shown in Fig. 19. On classical images, a SR value is estimated and will allow us quantifying the AO loop residuals. The coronagraphic image provides the final performance in terms of detectivity.

From the classical PSF, an SR has been computed: SR $= 90.3 \pm 2$ at 1589 nm. The error bars are estimated empirically from experience and knowledge of the system parameter accuracy. This SR can be translated into a global residual error: $\sigma_{\text{total}} = 81 \pm 10$ nm RMS. Knowing that the fitting error for an 0.85 arc sec seeing is estimated to $\sigma_{\text{fit}} = 60 \pm 10$ nm RMS. It leads to a residual RMS on corrected modes (by the AO system) $\sigma_{\text{corr}} = 54 \pm 14$ nm RMS, which is well within the specification and fully coherent with the simulation results $\text{SR}_{\text{sim}} = 89.8\%$, leading to $\sigma_{\text{corr,sim}} = 83$ nm RMS.

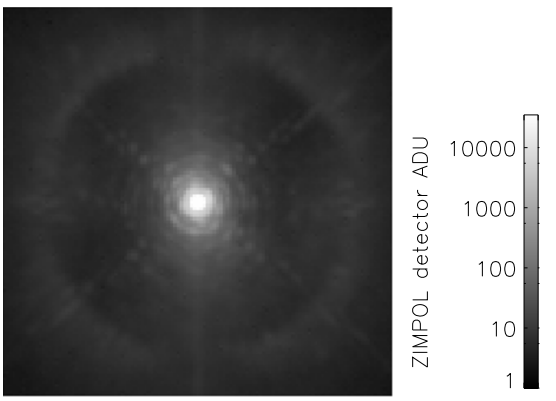

Fig. 20 SPHERE PSF in R band as during AIT period, obtained with nominal conditions of GS flux and atmospheric turbulence. The angular resolution obtained on this PSF is estimated at 17 mas in *X* direction and 20 mas in the other direction. The difference between *X* and *Y* axis is due to residual vibrations, for which the system is very sensitive at such FWHM.

Moreover, due to the visible capacities brought by the ZIMPOL instrument, the SPHERE system could demonstrate in laboratory and on turbulence simulator, the highest resolution reached by an astronomical instrument. Figure 20 shows a PSF obtained in lab in R band, on nominal turbulence conditions (0.85 arc sec seeing, 12-m/swind speed), and 9 magnitude. The AO correction allowed to reach a high level of correction. Of course, the SR is smaller than in H band (around 40%), but the angular resolution (measured by FHWM estimation) is estimated at 17 mas on the *X* axis and 20 mas on the *Y* axis. The difference between *X* and *Y* axis comes from the difference in jitter residual between *X* and *Y* axis, as estimated on SAXO data.

3.5.3 *Performance for faint guide stars*

The evolution of SPHERE performance with respect to flux is a vital behavior. A special care for the validation of this point has been taken. Figure 21 shows the evolution of SAXO performance (in terms of SR) for various SNR conditions. The

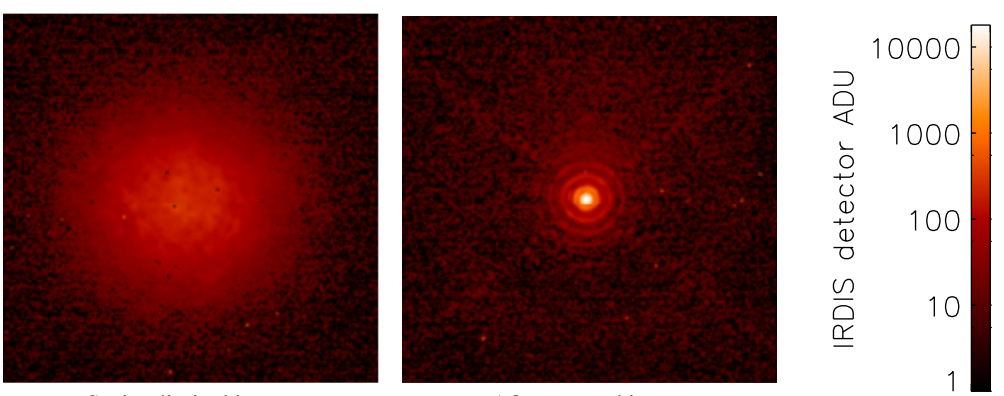

Fig. 19 Long exposure SPHERE PSF in H band during AIT period, obtained with nominal conditions of GS flux and atmospheric turbulence. Strehl ratio is given in H band, at 1.6 μm. (a) Image is acquired in seeing limited mode, no AO correction performed. (b) Image acquired with full AO correction, in nominal turbulence seeing conditions.

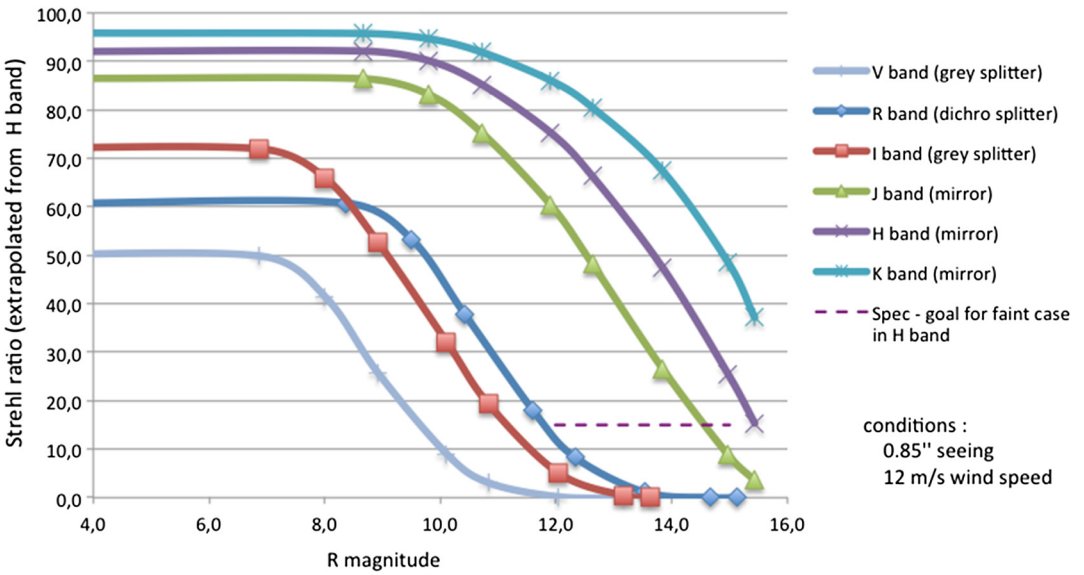

Fig. 21 Performance of SPHERE with respect to GS magnitude as measured in laboratory. Only the H performances have been measured (purple line), the performance at other wavelengths have been extrapolated from the H band measurement.

absolute value of R magnitudes has been computed from flux measured on VIS-WFS subapertures and system measured transmissions. The flux of the source used in laboratory during AIT is modified on a wide range, due to a tunable fiber coupling device. The performance of the system with respect to flux has therefore been tested in realistic conditions.

Only the H band performance has been experimentally measured for all magnitudes. The performance at other wavelengths has been derived from the H band measurement following the two following rules:

- The change in performance from one measurement to another follows a decrease due to wavelength. The SR at a wavelength λ_2 can be interpolated from the Strehl at a wavelength λ_1 by the relation: $\mathrm{SR}(\lambda_1) = \mathrm{SR}(\lambda_2)^{(\lambda_1/\lambda_2)^2}$.
- Changing the wavelength imposes a change in optical configuration for SPHERE and changing the beam splitter between ZIMPOL path and WFS path. A change of flux is therefore occurring.

It shows that ultimate performance is achieved (in H band) for magnitude fainter than 9 and that the performance smoothly drops down to 15% for magnitude down to 15.5. This limit magnitude is a crucial result for an AO system. This impressive result is due to the very good system transmission and the extreme performance of the WFS in terms of read-out noise (which is well below $1e^-$) and quantum efficiency. The fact

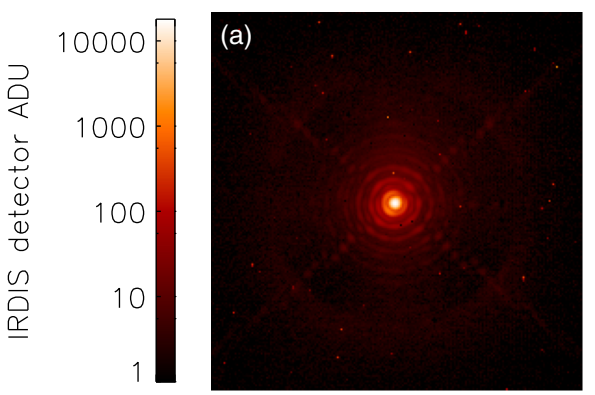

Wind speed [m/s]	12.5	30.0
Seeing [arcsec]	1.12	1.12
Strehl Ratio@H	85.5%	73.3%

Fig. 22 SPHERE PSF in poor turbulence conditions. (a) The long exposure PSF with high seeing conditions, at 1.12 arc sec. This seeing condition corresponds to the strong turbulence value, obtained by using both phase screens jointly. (b) The long exposure PSF with high seeing condition and high wind speed of 30 m/s. This higher value of wind speed is obtained by increasing the phase screen rotation speed.

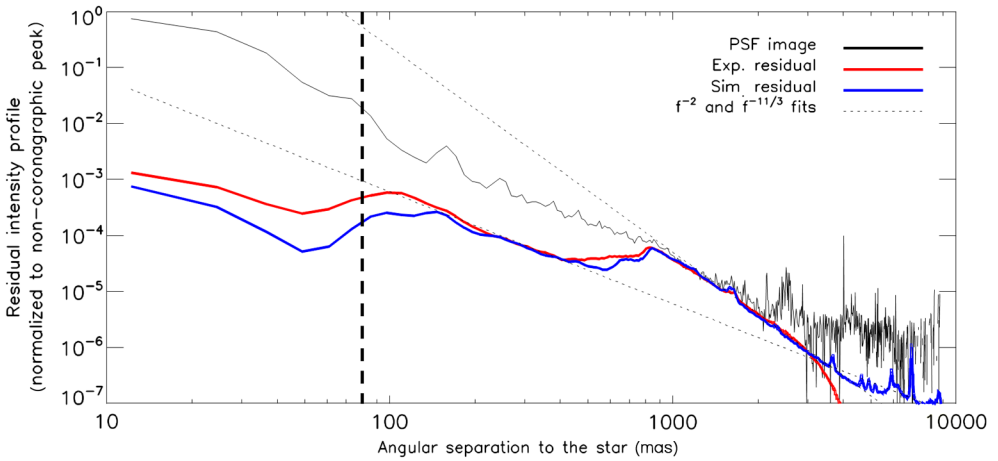

Fig. 23 SPHERE coronagraphic residual intensity profiles in nominal turbulence conditions and comparison with simulation. The simulation curves have been obtained by simulating the AO data at the same turbulence conditions than the experimental data. The vertical dashed line refers to the extension of the coronagraphic mask in the focal plane. The Lyot mask covers the central part close to optical axis.

that the WFS detector is a deep depletion device is the main contributor to this result.

3.5.4 *Performance in poor turbulence conditions*

In this section, the performance (as well as the robustness) of the system is studied in the poor condition regime, i.e., at a seeing of 1.12 arc sec and two wind speed values of 12.5 and 30 m/s. Despite some actuators in saturation (well handled by the anti-wind up and garbage collector processes), the loop was stable and robust during all the acquisition process (a few tens of minutes). The PSF corresponding to these conditions is shown in Fig. 22. The corresponding SR (H band) is estimated at 85.5% and 73.3%. The main effect of the high wind speed level is a smooth pattern of light residuals all over the corrected halo along the wind direction (vertical in the images). This smooth pattern can be partially removed by differential imaging techniques.

3.6 *Coronagraphic Imaging and Performance*

The last demonstration of SAXO performance is done using coronagraphic images. Figure 23 shows raw coronagraphic image profiles, compared to a full end-to-end simulation. The profiles are obtained by the azimuthal average of residual intensity of the coronagraphic images. The two profiles match quite well, both in terms of contrast level and in structure. In the corrected area up to 800 mas, the profile follows a f^{-2} law signature of the noise and wind speed residual errors. After the AO cutoff frequency, a $f^{-11/3}$ law is found with the correct level (for 0.85 arc sec seeing conditions). Only a very small over excitation is visible in the experimental data around 700 mas (less than a factor 1.5). It can be due to a WFS spatial filter a little bit larger in experimental data than in simulation and to the dead actuators. In any case, the coronagraphic shape is very well mastered and understood. It follows the simulation data demonstrating that the AO loop is doing exactly what it is supposed to do. Note that these data were acquired when only eight actuators

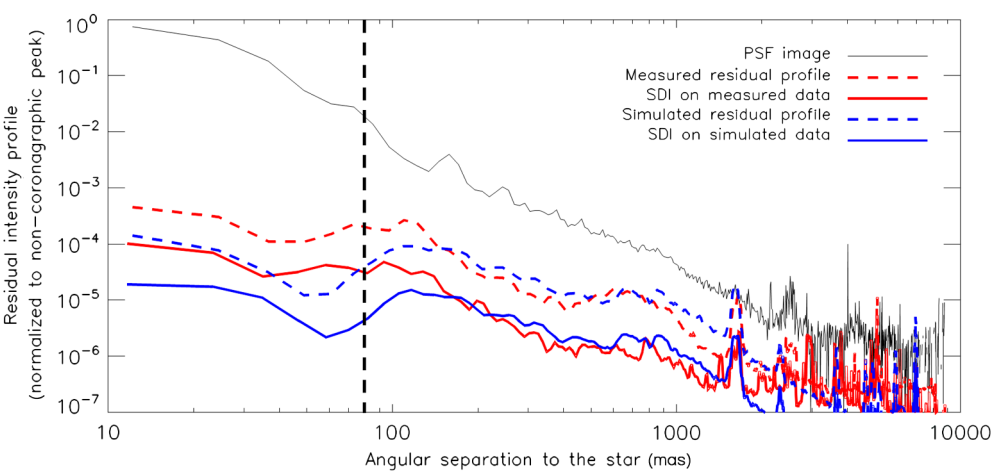

Fig. 24 SPHERE coronagraphic detectivity profiles in nominal turbulence conditions, resulting from spectral differential imaging. As in Fig. 23, the vertical dashed line stands for the size of the coronagraphic mask. All values of detection situated at smaller angular separations are therefore unusable.

were dead. The raw contrast degrades with the additional dead actuators (18 at the date of publication), but this has been solved by the use of dedicated masks presented in Sec. 2.3.4.

In addition, we study the detectivity curves shown in Fig. 24. The detectivity curves are the azimuthal RMS value of the residual intensity of the coronagraphic image. Once again, we compare experimental results and simulation. For detectivity aspect, the results depend on the exposure time (which will allow smoothing the residual turbulence speckle). In Fig. 24, we compare an experimental data with 10 and 3.4 s exposure time with simulated data. As expected, the detectivity curve is proportional to the square root of the exposure time in the non-corrected area (where the dominant noise is the pure speckle one). In the corrected area, things are more complex and the dependency with exposure time is less clear. Nevertheless, again a remarkable (for such kind of attenuation level and such a complex system) match can be noticed between simulation and experimental data. Finally, a spectral differential imaging (SDI) process is applied on both simulated and experimental data leading to solid line profiles in Fig. 24 and an SDI performance around 10^{-6} for the two exposure times considered here, as expected in SPHERE technical requirement.

4 Conclusion

The SPHERE instrument has been delivered to the VLT Observatory in mid-2014. SAXO, the extreme AO system of SPHERE, has followed a long integration period from late 2011 to the end of 2013 when the subsystem has been integrated to the full instrument. The performance reached by SAXO during AIT and shown in this article are fully compatible with the extreme imaging quality required for exoplanet direct imaging. The SR measured in laboratory with realistic star flux and turbulence reach 90% in H band, with around 80-nm residual aberrations. This performance ensures a very high quality for high contrast imaging, and SDI performances are demonstrated in laboratory down to detectivity values of 10^{-6}.[42,43] The mid-term perspective of this work is to improve the AO components, in particular, the high order DM. The main limit is a risk of quick degradation (both in losing additional actuators and having an evolution with time of the shape at rest), making the operation of the system impossible. In a more long term, the possible evolution of the WFS to a pyramid would permit a strong improvement in term of aliasing and sensitivity. Note that this improvement would require a strong modification of the system (both in hardware and software) and is purely hypothetic today. The perspective in terms of performance would benefit from a better calibration of the internal defect of the instrument. Even if the requirement has been met with the actual system, the very actual postfocal techniques of NCPA calibration (COFFEE, ZELDA) are very promising and are able to provide improved performance to the SPHERE system once integrated. The compensation of the NCPA should also be improved on SPHERE, taking benefit of all the existing techniques of dark hole and suppressing the light residuals in the focal plane, hence beating the diffraction limit for a reduced area. Among them, electric field conjugation has been tested experimentally on the system during 2015 bringing an unprecedented gain in contrast.

Acknowledgments

This work was partly funded by the European Commission under FP7 Grant Agreement No. 312430 Optical Infrared Coordination Network for Astronomy, and by the Office National d'Etudes et de Recherches Aerospatiales (ONERA) in the frame of the NAIADE Research Project. SPHERE is an instrument designed and built by a consortium consisting of IPAG, MPIA, LAM, LESIA, Laboratoire Fizeau, INAF, Observatoire de Geneve, ETH, NOVA, ONERA and ASTRON in collaboration with ESO. The authors want to thank ESO and SPHERE consortium for implication and participation to AIT of SAXO instrument. The HODM has been provided by the CILAS company through a joint research and development effort under funding from the European Commission Sixth Framework Programme as part of the Optical Infrared Coordination Network for Astronomy (OPTICON) under Grant No. RII3-Ct-2004-001566 (2004-2008).

References

1. G. Chauvin et al., "A giant planet candidate near a young brown dwarf. Direct VLT/NACO observations using IR wavefront sensing," *Astronom. Astrophys.* **425**, L29–L32 (2004).
2. G. Rousset et al., "NAOS, the first AO system of the VLT: on-sky performance," *Proc. SPIE* **4839**, 140 (2003).
3. R. Dekany et al., "PALM-3000: exoplanet adaptive optics for the 5 m hale telescope," *Astrophys. J.* **776**, 130.
4. F. Martinache et al., "On-sky speckle nulling demonstration at small angular separation with SCExAO," *Publ. Astron. Soc. Pac.* **126**, 565–572 (2014).
5. L. M. Close et al., "First closed-loop visible AO test results for the advanced adaptive secondary AO system for the Magellan telescope: MagAO's performance and status," *Proc. SPIE* **8447**, 84470X (2012).
6. S. Esposito et al., "LBT AO on-sky results," in *Second Int. Conf. on Adaptive Optics for Extremely Large Telescopes*, id.3, p. 3 (2011).
7. T. Fusco et al., "Final performance and lesson-learned of SAXO, the VLT-sphere extreme AO: from early design to on-sky results," *Proc. SPIE* **9148**, 91481U (2014).
8. B. Macintosh et al., "First light of the Gemini Planet Imager," *Proc. Natl. Acad. Sci.* **111**, 12661–12666 (2014).
9. J.-L. Beuzit et al., "Sphere: a 'planet finder' instrument for the VLT," *Proc. SPIE* **7014**, 701418 (2008).
10. O. Guyon, "Limits of adaptive optics for high-contrast imaging," *Astrophys. J.* **629**, 592–614 (2005).
11. D. Mouillet et al., "Sphere: a 'planet finder' instrument for the VLT," in *Science with the VLT in the ELT Era*, E. S. O. Alan Moorwood, Ed., pp. 337–341, Springer, The Netherlands (2009).
12. K. Dohlen et al., "The infra-red dual imaging and spectrograph for SPHERE: design and performance," *Proc. SPIE* **7014**, 70143L (2008).
13. R. U. Claudi et al., "SPHERE IFS: the spectro differential imager of the VLT for exoplanets search," *Proc. SPIE* **7735**, 77350V (2010).
14. R. Roelfsema et al., "The ZIMPOL high contrast imaging polarimeter for sphere: system test results," *Proc. SPIE* **9147**, 91473W (2014).
15. R. Soummer, "Apodized pupil Lyot coronagraphs for arbitrary telescope apertures," *Astrophys. J. Lett.* **618**, L161–L164 (2005).
16. A. Boccaletti et al., "The four-quadrant phase mask coronagraph. IV. First light at the very large telescope," *Publ. Astron. Soc. Pac.* **116**, 1061–1071 (2004).
17. M. D. Perrin et al., "The structure of high Strehl ratio point-spread functions," *Astrophys. J.* **596**, 702–712 (2003).
18. G. Montagnier et al., "Pupil stabilization for sphere's extreme AO and high performance coronagraph system," *Opt. Express* **15**(23), 15293–15307 (2007).
19. C. Petit et al., "Hybrid LQG/integrator control for the VLT extreme AO system sphere," in *IEEE Int. Conf. on Control Applications*, pp. 878–883 (2010).
20. L. A. Poyneer and B. A. Macintosh, "Wavefront control for extreme adaptive optics," *Proc. SPIE* **5169**, 190 (2003).
21. T. Fusco et al., "Closed-loop experimental validation of the spatially filtered Shack-Hartmann concept," *Opt. Lett.* **30**(11), 1255–1257 (2005).
22. P. Baudoz et al., "The differential tip-tilt sensor of sphere," *Proc. SPIE* **7735**, 77355B (2010).
23. E. Fedrigo et al., "SPARTA for the VLT: status and plans," *Proc. SPIE* **7736**, 77362I (2010).

24. M. Suárez Valles et al., "SPARTA for the VLT: status and plans," *Proc. SPIE* **8447**, 84472Q (2012).
25. E. Gendron and P. Lena, "Astronomical adaptive optics. 1: modal control optimization," *Astronom. Astrophys.* **291**, 337–347 (1994).
26. C. Petit et al., "Optimisation of the control laws for the SPHERE XAO system," *Proc. SPIE* **7015**, 70151D (2008).
27. R. N. Paschall and D. J. Anderson, "Linear quadratic Gaussian control of a deformable mirror adaptive optics system with time-delayed measurements," *Appl. Opt.* **32**, 6347–6358 (1993).
28. C. Petit et al., "First laboratory validation of vibration filtering with LQG control law for adaptive optics," *Opt. Express* **16**(1), 87–97 (2008).
29. S. Meimon et al., "Tip–tilt disturbance model identification for Kalman-based control scheme: application to XAO and ELT systems," *J. Opt. Soc. Am. A* **27**(11), A122–A132 (2010).
30. M. Nicolle et al., "Improvement of Shack-Hartmann wave-front sensor measurement for extreme adaptive optics," *Opt. Lett.* **29**(23), 2743–2745 (2004).
31. C. Robert et al., "Improvement of phase diversity algorithm for non-common path calibration in extreme AO context," *Proc. SPIE* **7015**, 70156A (2008).
32. B. A. Macintosh et al., "The Gemini Planet Imager: from science to design to construction," *Proc. SPIE* **7015**, 701518 (2008).
33. C. Petit et al., "Sphere extreme AO control scheme: final performance assessment and on sky validation of the first auto-tuned LQG based operational system," *Proc. SPIE* **9148**, 91480O (2014).
34. E. Hugot, G. R. Lemaître, and M. Ferrari, "Active optics: single actuator principle and angular thickness distribution for astigmatism compensation by elasticity," *Appl. Opt.* **47**(10), 1401–1409 (2008).
35. E. Hugot et al., "Active optics methods for exoplanet direct imaging. Stress polishing of supersmooth aspherics for VLT-SPHERE planet finder," *Astronom. Astrophys.* **538**, A139 (2012).
36. S. Meimon, C. Petit, and T. Fusco, "The Slope-Oriented Hadamard Scheme for in-lab or on-sky interaction matrix calibration" in *Second International Conference on Adaptive Optics for Extremely Large Telescopes*, p. 65 (2011).
37. T. Fusco et al., "NAOS on-line characterization of turbulence parameters and adaptive optics performance," *J. Opt. A: Pure Appl. Opt.* **6**(6), 585 (2004).
38. V. N. Mahajan, "Zernike annular polynomials for imaging systems with annular pupils," *J. Opt. Soc. Am.* **71**, 75–85 (1981).
39. J.-F. Sauvage et al., "Calibration and precompensation of noncommon path aberrations for extreme adaptive optics," *J. Opt. Soc. Am. A* **24**(8), 2334–2346 (2007).
40. P. Martinez et al., "Speckle temporal stability in XAO coronagraphic images-II. Refine model for quasi-static speckle temporal evolution for VLT/SPHERE," *Astronom. Astrophys.* **554**, A41 (2013).
41. A. Vigan et al., "Photometric characterization of exoplanets using angular and spectral differential imaging," *Mon. Not. R. Astro. Soc.* **407**, 71–82 (2010).
42. D. Mesa et al., "Performance of the VLT planet finder SPHERE. II. Data analysis and results for IFS in laboratory," *Astronom. Astrophys.* **576**, A121 (2015).
43. A. Zurlo et al., "Performance of the VLT planet finder SPHERE-I. Photometry and astrometry precision with IRDIS and IFS in laboratory," *Astronom. Astrophys.* **572**, A85 (2014).

Jean-Francois Sauvage is an adaptive optics scientist. Since his PhD in 2007, his research work has been focused on high performance AO systems and in particular on the thematics of the calibration of XAO system for exoplanet imaging. His work on the framework of the SPHERE instrument consisted in the integration of the whole XAO system SAXO, in lab and on-sky, as well as the global operation of AO with the whole instrument SPHERE.

Biographies for the other authors are not available.